

Effect of deep cryogenic treatment on microstructure and mechanical properties of AlCoCrFeNi_{2.1} eutectic high-entropy alloy

Si-ruo Zhang^{1,2}, Cheng-hao Liu^{1,2}, Hao Qi^{1,2}, Hao-kai Wu^{1,2}, Guang-yu Yang³, Ting-shuai Tan³, **Ying-dong Qu^{1,2}, and *Guang-long Li^{1,2}

1. School of Materials Science and Engineering, Shenyang University of Technology, Shenyang 110870, China

2. Technical Innovation Center for Lightweight and High Performance Metal Materials of Liaoning Province, Shenyang University of Technology, Shenyang 110870, China

3. China Coal Science and Industry Group Shenyang Research Institute Co., Ltd., Shenyang 110013, China

Copyright © 2025 Foundry Journal Agency

Abstract: As a typical eutectic high-entropy alloy (EHEA), AlCoCrFeNi_{2.1} exhibits excellent casting properties. However, the imbalance between strength and plasticity hinders its application as an advanced structural material. In order to address this challenge, deep cryogenic treatment (DCT) as a new process applied in the field of EHEAs was proposed in this study. The effects of different DCT times on the microstructure and mechanical properties of AlCoCrFeNi_{2.1} EHEAs were studied, mainly focusing on the flake structure of FCC+B2 layer. The experimental results suggest that with the extension of the DCT time, the dislocation density in the FCC phase increases significantly. The spherical BCC precipitate phase is generated within the B2 phase, and the average size of this newly generated precipitate phase gradually decreases. Increasing the number of dislocations and precipitate phases is of great significance to improve the mechanical properties. The AlCoCrFeNi_{2.1} EHEA exhibits excellent comprehensive mechanical properties after DCT for 36 h. Compared with the as-cast state, the tensile strength at room temperature reaches 1,034.51 MPa, increased by 5.74%. The plasticity reaches 21.72%, which is increased by 11.79%. The results show that the tensile strength and ductility of AlCoCrFeNi_{2.1} EHEAs are balanced and improved after DCT, which are more suitable as advanced structural materials. In addition, the introduction of the DCT process to EHEAs solves the problem of environmental pollution caused by traditional heat treatment process. This study provides useful guidance for using the DCT process to strengthen the mechanical properties of “lamellar + block” type EHEAs.

Keywords: deep cryogenic treatment (DCT); eutectic high-entropy alloy (EHEA); dislocation; precipitate; mechanical properties

CLC numbers: TG146.21

Document code: A

Article ID: 1672-6421(2025)03-352-11

1 Introduction

AlCoCrFeNi_{2.1} eutectic high-entropy alloy (EHEA) has the characteristics of both eutectic alloy and high-entropy alloy. Due to its good casting fluidity, high

breaking strength, and high wear resistance, it has excellent application prospects in the preparation of special environmental materials such as ship propellers, icebreakers, and deep-sea drill bits^[1-4]. In engineering applications, the balance between strength and plasticity is critical to improving the safety and longevity of metal structural materials^[5]. However, the strength and plasticity of cast alloy materials are usually mutually restrictive. Therefore, how to develop a high-entropy alloy with good casting fluidity and high strength plasticity is an important problem in the field of new materials.

At present, there are three mainstream methods to improve the strength and plasticity of high-entropy alloys. (I) Optimizing the alloy composition by adding

*Guang-long Li

Ph. D., Associate Professor and Doctoral Supervisor. His research interests mainly focus on carbon fibers reinforced aluminum matrix composites, high entropy alloys, and hydrogen storage materials. To date, he has published more than 30 papers.

E-mail: liguanglong1990@163.com

**Ying-dong Qu

E-mail: quydong@sut.edu.cn

Received: 2024-03-11; Revised: 2024-07-03; Accepted: 2024-11-18

elements. (II) Utilizing new preparation technologies such as high-energy ball milling, plasma spraying, and rapid solidification. (III) Using heat treatment process to optimize the grain size, grain boundary characteristics, and precipitate phase number of high-entropy alloys to improve the mechanical properties of the alloys. Huo et al.^[6] found that by adding of 0.4at.% Zr to the CoCrFeNi alloy, a eutectic structure composed of FCC phase and Laves phase was formed, which can effectively delay high-temperature creep and thus has great potential in high-temperature resistant materials. Tan et al.^[7] found that the alternating arrangement of FCC and tetragonal Mn₇Pd₃ structures in the CoCrFeNiMn alloy with Pd would lead to the weakening of the interfacial energy anisotropy, resulting in a “seaweed-like” eutectic structure. He et al.^[8] found that when 0.25at.% Nb was added to the CoCrFeNi alloy, a lamellar structure composed of an FCC phase and a hard HCP phase was formed in the CoCrFeNiNb_x high-entropy alloy with good strong plasticity. The compressive yield strength and compressive strain of CoCrFeNiNb_{0.25} can reach 2,024.6 MPa and 38.8%, respectively. Tao et al.^[18] prepared CoNiCrMoNb high-entropy alloys by plasma spraying, and the results showed that the hardness and wear resistance of high-entropy alloys were improved with the increase of amorphous alloy content in the matrix as the spraying power increased. Nassar et al.^[9] prepared AlCoCrFeNi_{2.1} EHEA by rapid solidification technology. It was found that with the increase of cooling rate, the microstructure of AlCoCrFeNi_{2.1} EHEA gradually changed from a regular eutectic to a “colony-like” eutectic, which reduced the interlayer spacing and improved the microhardness. Peng et al.^[14] annealed the as-cast AlCoCrFeNi_{2.1} EHEA and found that the precipitated phase (CoCrFe phase) was produced in the B2 phase after annealing at 800 °C for 10 h. The tensile strength and compressive strength were improved from 1,007 and 1,847 MPa to 1,173 and 2,850 MPa, respectively. Sheng et al.^[15] annealed as-cast Al_{0.5}CoCrFeCuNi high-entropy alloys and found that the compressive fracture strength of AlNi-rich BCC phase and AlCu-rich nanophase precipitation was increased by 66% after annealing at 600 °C for 24 h. However, for EHEA castings, the addition of alloying elements is prone to segregation, which is not conducive to the manufacture of large ingots. The use of traditional heat treatment methods, such as annealing or quenching, will reduce the dimensional accuracy of castings and limit the application of high-entropy alloy castings in aviation, navigation, and precision instruments^[31].

Deep cryogenic treatment (DCT) is a method that uses liquid nitrogen as a cooling medium to instantly cool the alloy to a temperature much lower than room temperature (-196 °C). It can significantly improve the grain boundary distribution, dislocation density and the number of precipitated phases of high entropy alloy, so as to improve the mechanical properties of the alloy^[11]. Previous studies of our research group have shown that after DCT of Al_xCrFe₂Ni₂ series high-entropy alloys for different times, dislocations and precipitates with different densities will appear in high-entropy alloys. Benefiting from

dislocation strengthening and second phase strengthening, the compressive strength of Al_xCrFe₂Ni₂ high-entropy alloys after DCT is significantly improved^[12,29]. In addition, the DCT process is simpler and more economical than the traditional heat treatment process. DCT does not suffer from the issue of insufficient hardenability and is suitable for the strengthening treatment of castings with various sizes. In general, the interaction of multiple elements in EHEAs prepared by casting is limited, resulting in poor plasticity. The DCT process can make the lattice distortion in EHEAs more serious, increase the dislocation density and the number of precipitated phases in the eutectic structure, and refine the bulk structure of the non-eutectic structure. DCT can simultaneously enhance the strength and plasticity of EHEA, achieving a balance between high strength and high plasticity. This further drives rapid industrialization and meets the growing demand for advanced structural materials.

In this study, the DCT process of AlCoCrFeNi_{2.1} EHEA for different times was studied, and the influence of DCT time on the microstructure and mechanical properties of EHEAs was analyzed in detail. The mechanism of synchronous improvement of strength and plasticity of EHEAs after DCT was explained. This study can provide an important research basis for the production and application of EHEA castings with strength-plasticity balance.

2 Experiment

The EHEAs with nominal composition of AlCoCrFeNi_{2.1} (atomic percentage) were prepared by using a vacuum arc melting furnace (BTFJ21-03) in a zirconium-absorbing high-purity argon atmosphere. The raw materials used for EHEA were Al, Co, Cr, Fe, and Ni, each with a purity of at least 99.9wt.%. To ensure uniformity of ingredients, each ingot was turned over and remelted for five times, with electromagnetic stirring during the last two melting. Finally, the molten alloy was poured into a hemispherical water-cooled copper mold by gravity, forming an EHEA button ingot. Before the DCT process, the samples were placed in a sealed plastic pipe to reduce the error and prevent the formation of hexagonal AlN impurities on the surface of the samples. As shown in Fig. 1(a), the samples were sealed and immersed in liquid nitrogen. The liquid nitrogen tank has an outer insulating layer that can keep the temperature constant at about 77 K. The AlCoCrFeNi_{2.1} EHEA samples were soaked for 0, 12, 24, and 36 h, respectively. These samples were named AC, DCT-12, DCT-24 and DCT-36. The samples were taken out of liquid nitrogen and placed in a water bath at 298 K for 1 h to ensure that the temperature of all samples was restored simultaneously and uniformly. The schematic diagram of DCT process is shown in Fig. 1(b).

The microstructure and elemental distribution of the alloy were investigated using scanning electron microscopy (SEM, Gemini 300) equipped with X-ray energy dispersive spectroscopy (EDS, Oxford Aztec). The phase structure

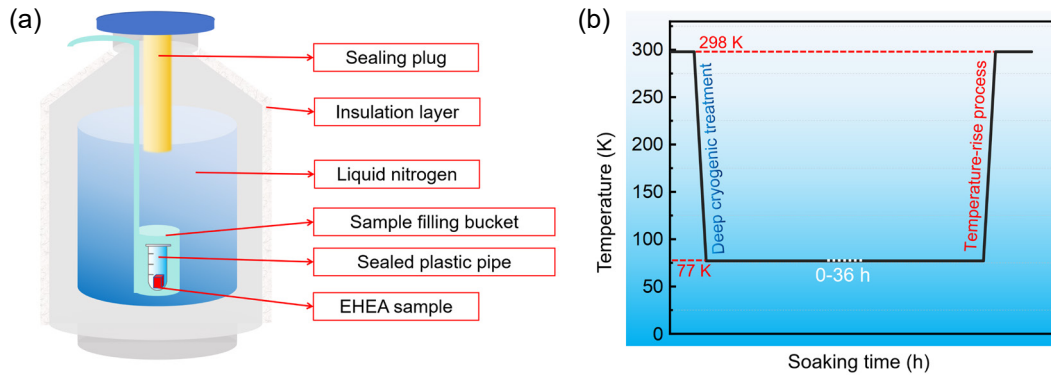


Fig. 1: Schematic diagram of a DCT device (a) and flowchart of the DCT process (b)

of the EHEA was analyzed using an X-ray diffractometer (XRD, Shimadzu 7000) with Cu-K α . The scanning range was 20°–100°, and the scanning rate was 2°·min⁻¹. After the DCT process, the sample surface was mechanically ground using SiC sandpapers. Subsequently, an electrolytic polishing and etching instrument (Naibo EP-06) was used to remove the scratch layer caused by the previous mechanical grinding. The corrosive liquid was a mixed solution of 90% C₂H₅OH and 10% HClO₄ by volume. The microstructure morphology was observed using scanning electron microscopy (SEM, Gemini 300) equipped with EBSD. Detailed analysis was performed using Channel 5 and Aztec Crystal data analysis software. TEM samples were prepared using an ion thinning machine (Gatan 691) after mechanical grinding. Transmission electron microscopy (TEM, JEM 2100) was used to characterize the microstructure changes before and after DCT.

Dog-bone tensile specimens with the length of 7 mm, the width of 4 mm, and the thickness of 2 mm were fabricated by electrical discharge machining (EDM). Tensile tests were performed at room temperature using an electronic universal testing machine (MTS-E45) equipped with an extensometer. Before the tensile tests, the samples were mechanically polished to remove the oxide skin and cleaned by ultrasonic vibration. In order to ensure the accuracy, the tensile rate was constant at 1×10⁻³ s⁻¹, and the tensile test at each DCT time was repeated for at least three groups. The fracture morphology of each group after tensile test was observed by a scanning electron microscope (SEM, Gemini 300).

3 Results

3.1 Microscopic observation

The XRD patterns in Fig. 2(a) show that AlCoCrFeNi_{2.1} EHEAs do not produce new diffraction peaks after different DCT times. Figure 2(b) provides a local magnification image of the diffraction peaks, which clearly shows that the FCC diffraction peaks of AlCoCrFeNi_{2.1} EHEAs shift to the right after DCT. The degree of shift of the diffraction peak increases with the DCT time. This phenomenon indicates that the compressive stress caused by DCT has a promoting effect on lattice distortion. From the as-cast state to DCT-36, the offset angles between the adjacent two groups are 0.42, 0.16, 0.14, respectively, showing a decreasing trend. Figure 2(c) shows the lattice constants of the most representative diffraction peaks (111) and (110) of FCC and B2 phases after DCT at different times calculated by the Bragg formula.

The SEM image in Fig. 3 shows the microstructure of as-cast AlCoCrFeNi_{2.1} EHEA. The eutectic structure with lamellar structure in Fig. 3(a) is composed of FCC phase and B2 phase alternately. The non-eutectic structure of coarse dendrite structure contains short rod-like B2 phase. EDS analysis shows that the B2 phase is rich in Al and Ni, and the FCC phase is rich in Fe, Co, and Cr. The SEM image of Fig. 4 shows the microstructure of AlCoCrFeNi_{2.1} EHEA after DCT for 36 h. After DCT-36, the lamellar structure of the eutectic structure maintains a parallel structure, which is similar to the as-cast microstructure. The bulk B2 phase in the non-eutectic structure

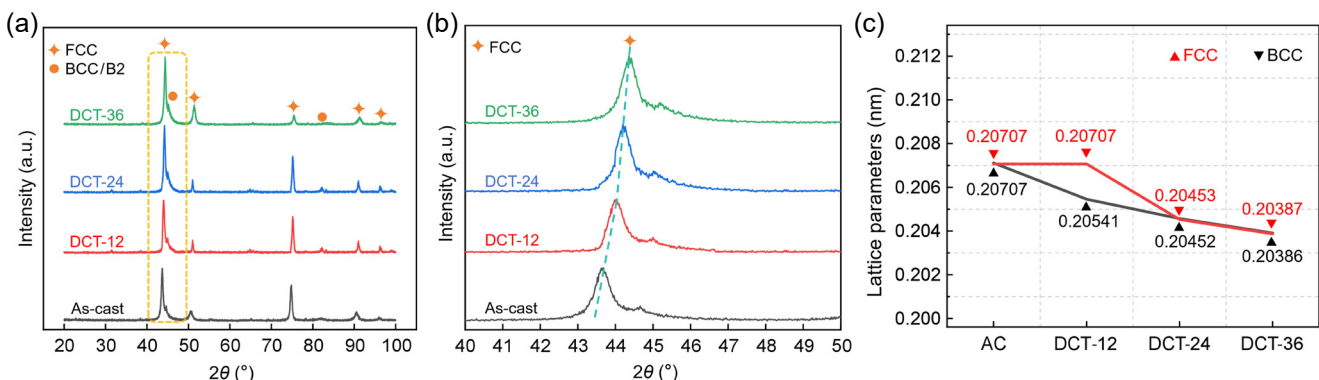


Fig. 2: XRD patterns and lattice parameter variation diagram: (a) XRD patterns of cast AlCoCrFeNi_{2.1} EHEA after different DCT times; (b) local magnification of XRD pattern in (a); (c) lattice parameters of various phases in EHEA under different DCT times

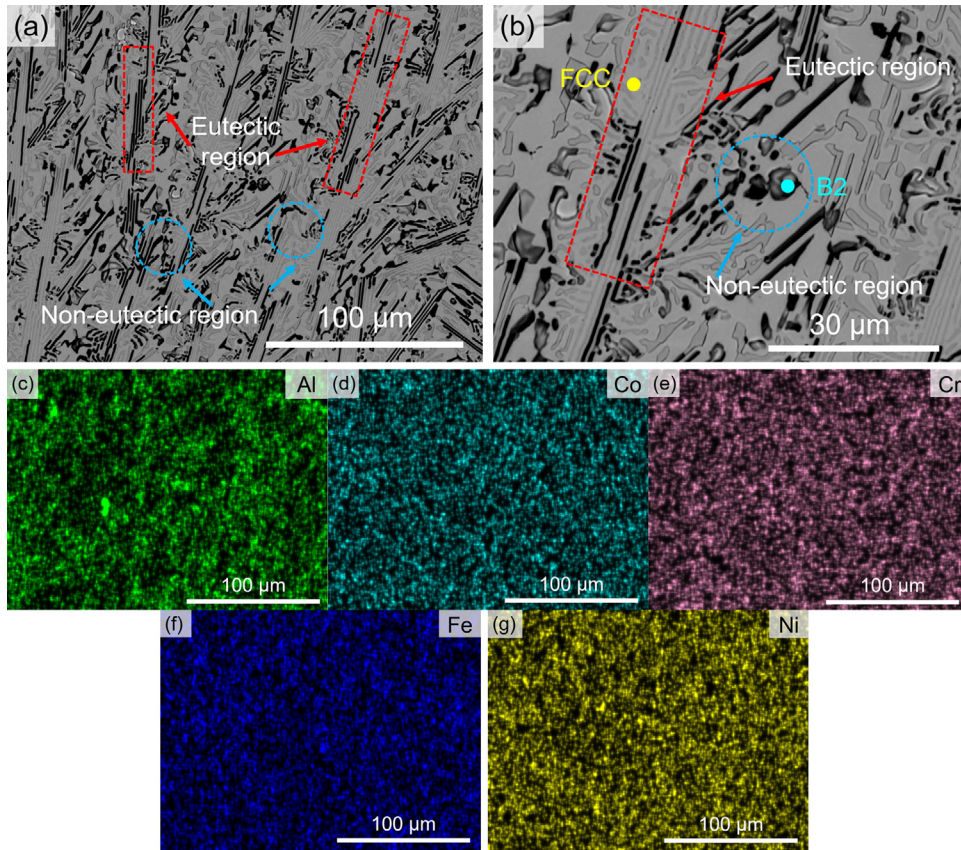


Fig. 3: Microstructure and element distribution in as-cast $\text{AlCoCrFeNi}_{2.1}$ EHEA: (a-b) SEM images of the as-cast $\text{AlCoCrFeNi}_{2.1}$ EHEA; (c-g) element distribution of Al, Co, Cr, Fe, and Ni in as-cast $\text{AlCoCrFeNi}_{2.1}$ EHEA

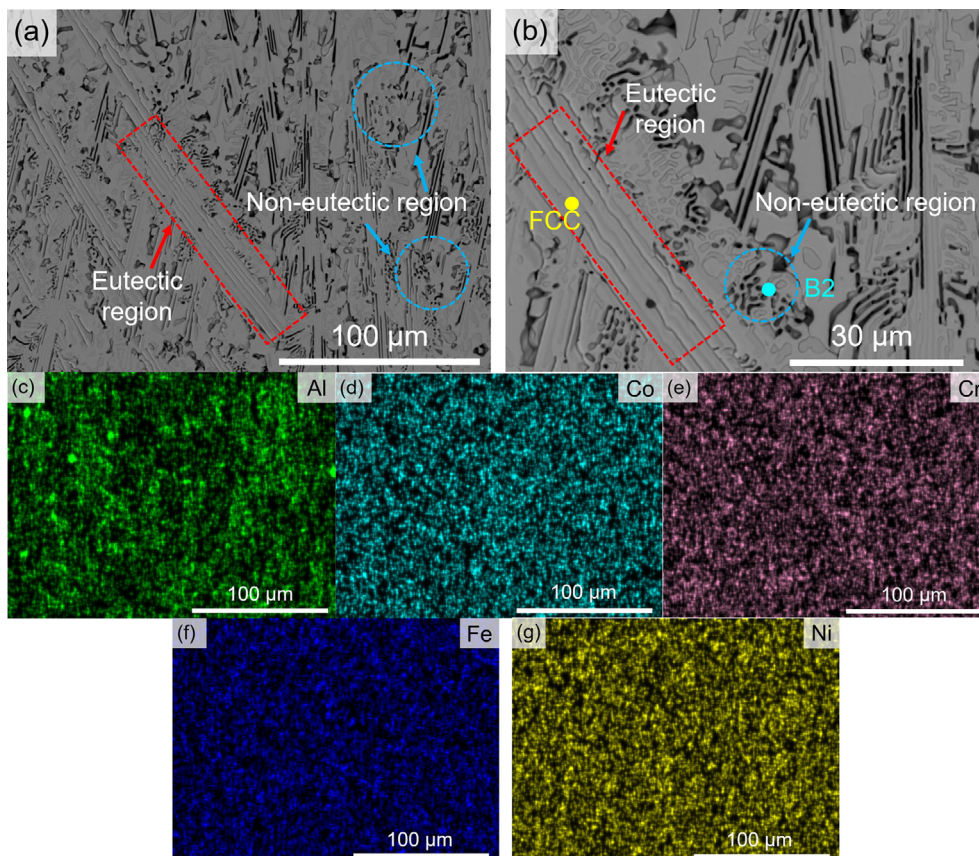


Fig. 4: Microstructure and element distribution in $\text{AlCoCrFeNi}_{2.1}$ EHEA after DCT-36: (a-b) SEM images; (c-g) element distribution of Al, Co, Cr, Fe, and Ni

will be broken to a certain extent. After DCT, each element shows uniform distribution and does not cause obvious element segregation.

The EBSD results in Fig. 5 are used to characterize the changes in microstructure, phase distribution, and stress of EHEA samples over different DCT times. Figures 5(a1)–(a4) show the phase distribution, and Figs. 5(b1)–(b4) present the Kernel average misorientation (KAM) map indicating the changes in strain. As shown in Figs. 5(a1)–(a4), the lamellar structure of FCC+B2 in the sample remains stable during the DCT process. FCC and B2 phases account for 76.06% and 23.94% in as-cast EHEA, respectively. After DCT-36, these proportions change slightly to 75.61% and 24.39%, indicating that large-scale phase changes do not occur during DCT. DCT increases the stress inside the EHEAs and causes different degrees of microplastic deformation in the eutectic and non-eutectic structures. The plastic deformation of the alloy

under low stress is called microplastic deformation. The region with higher KAM values represents a higher stress and shows a denser dislocation distribution [22]. Figures 5(b1)–(b4) show that the KAM value gradually increases with the extension of DCT time. KAM can reflect the density distribution of geometrically necessary dislocations (GNDs) quantized by local orientation differences, confirming that the dislocation density in AlCoCrFeNi_{2,1} EHEA increases with the extension of DCT time. Figures 5(c1)–(c4) show the average value of KAM, which is 0.63 in the as-cast state. With the extension of DCT time, the average value of KAM gradually increases to 1.95, 3.61, and 3.79. However, the growth trend has slowed down significantly, which further shows that there is a limit value of compressive stress introduced by DCT.

Figure 6(a) shows the bright field TEM image of the as-cast AlCoCrFeNi_{2,1} EHEA. A small number of dislocations are observed due to rapid cooling during the arc melting process.

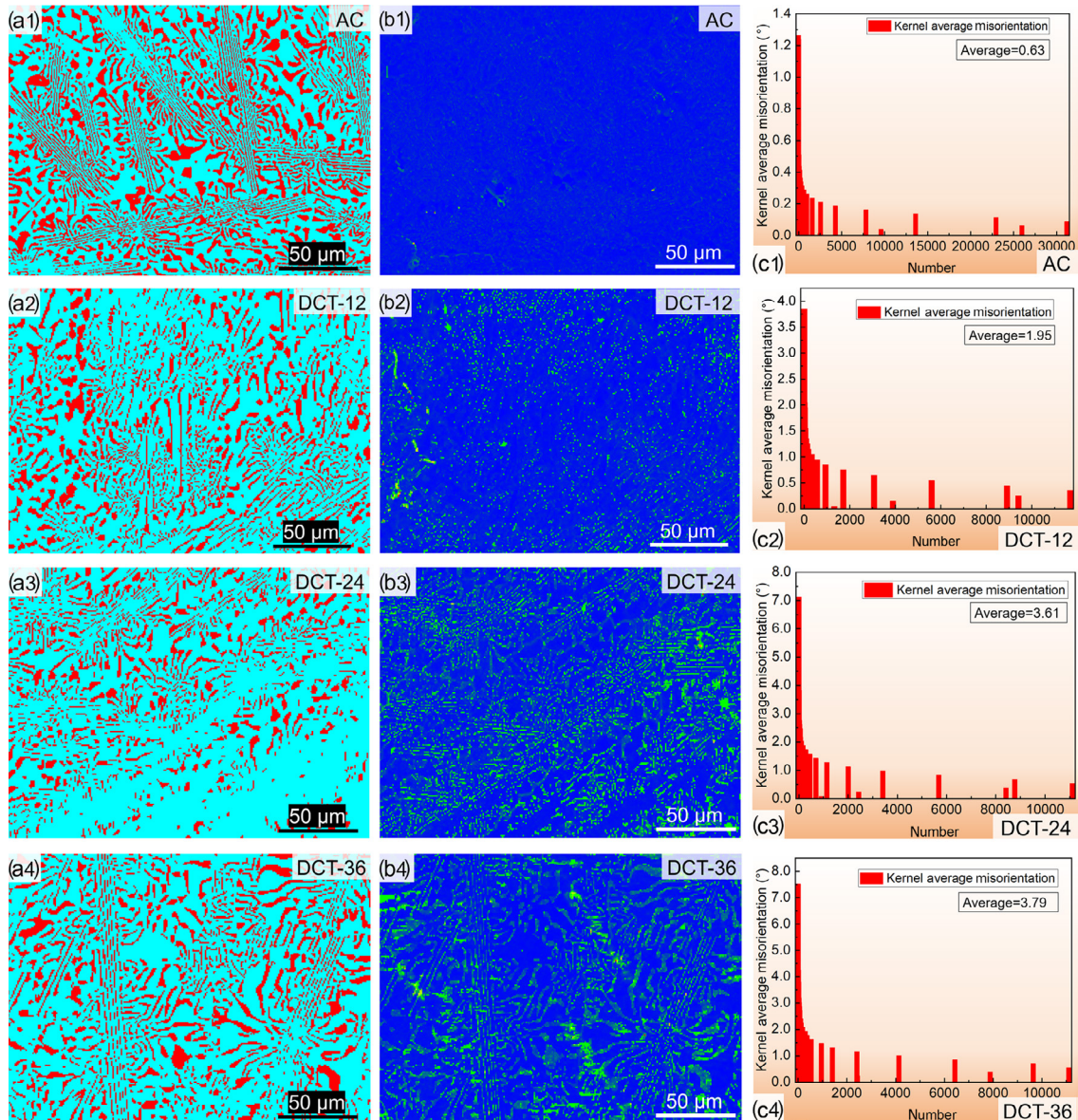


Fig. 5: EBSD images of the microstructure of AlCoCrFeNi_{2,1} EHEA as-cast (a1–c1) and DCT for 12 (a2–c2), 24 (a3–c3), and 36 h (a4–c4): (a1–a4) phase distribution images; (b1–b4) KAM images; (c1–c4) KAM data histogram and average KAM value

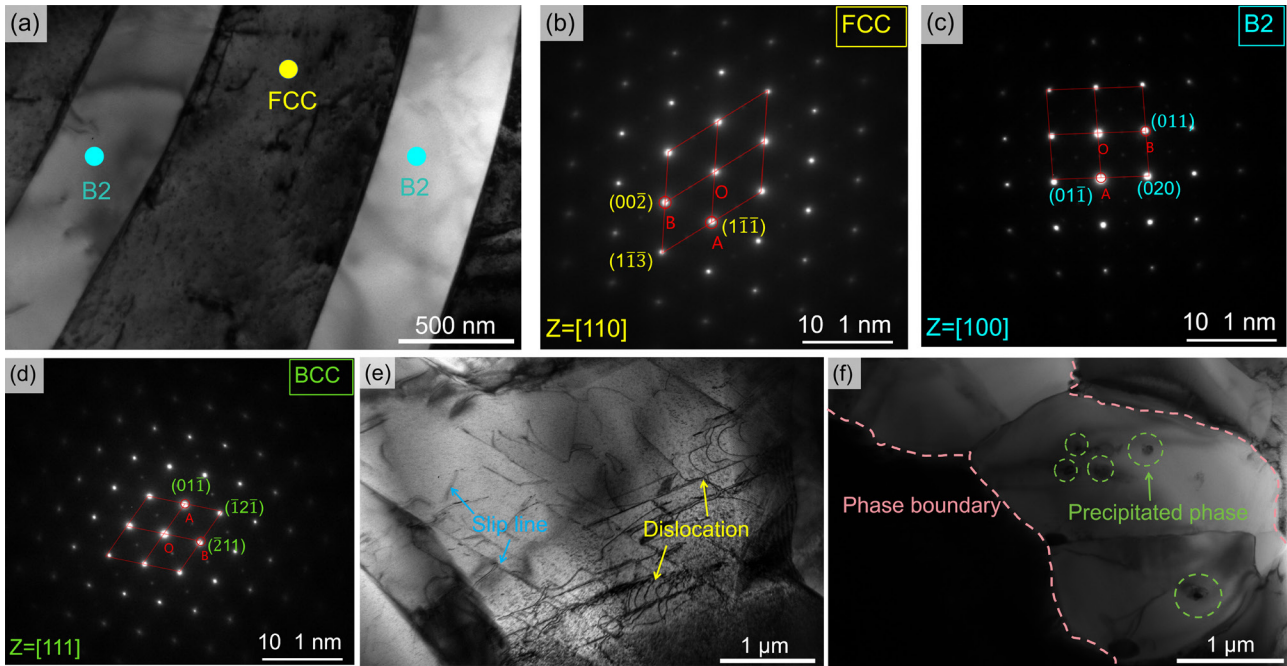


Fig. 6: TEM images of EHEA samples: (a) as-cast; (b-d) diffraction spot images of as-cast sample; (e-f) after DCT-12

There is no precipitated phase in the as-cast $\text{AlCoCrFeNi}_{2.1}$ EHEA. The eutectic structure presents a layered morphology, which is composed of alternating B2 and FCC phases. The selected area electron diffraction spots (SAED) in Fig. 6(b) and Fig. 6(c) confirm that the black area is FCC phase and the white area is B2 phase. In Fig. 6(e), compared with the as-cast $\text{AlCoCrFeNi}_{2.1}$ EHEA, the density of dislocations after DCT-12 is significantly increased. There are short linear low-density dislocations in FCC matrix. In Fig. 6(f), large-sized precipitates begin to appear in the B2 matrix. The diffraction point in Fig. 6(d) confirms that the precipitated phase is BCC phase.

The presence of high-density dislocations in the FCC phase can be observed in the microstructure of DCT-24, as shown in Fig. 7(a). It has also been observed that the dislocation line gradually changes from short line to network with the increase of DCT time^[29]. In addition, in Fig. 7(b), a significant increase in the number of precipitates in the B2 matrix and a decrease in the average size of precipitates are also observed in the microstructure of DCT-24. In Figs. 7(c)-(d), the dislocation density further increases after DCT-36. Many dislocation tangles are intertwined to form dislocation networks and dislocation wall structures. The size of the newly generated precipitates decreases and the number continues to increase. The spherical precipitate is more evenly distributed in the B2 matrix. The dislocation network filled in the FCC phase also promotes the formation of precipitates. Some of the precipitates are embedded in the FCC matrix surrounded by dislocation networks.

3.2 Mechanical properties

In Fig. (8), the tensile stress-strain curve shows that there are significant differences in fracture stress and strain before and after DCT. The ductility of alloys is significantly increased

with a longer DCT time. Compared with as-cast $\text{AlCoCrFeNi}_{2.1}$ EHEA, it exhibits excellent mechanical properties after DCT-36. The tensile strength increases from 978.32 MPa to 1,034.51 MPa and the tensile strain increases from 19.43% to 21.72%. Figures 9(a) and (b) show that the fracture morphology before and after DCT is similar, which is characterized by river-like cracks (groove-like microstructure) and brittle fractures (flat layered or reticular microstructure). The dimples on the fracture surface contain pit structures with different diameters and densities. In contrast, the fracture surface after DCT-36 in Fig. 9(c) shows a relatively low pore density. The high-rate scanning microscope image in Fig. 9(d) shows that the fracture surface is mainly composed of dimples with the size of 0.5–1.5 μm . The increase in the density of the dimple leads to a significant increase in the plasticity of the EHEAs.

4 Discussion

4.1 Effect of DCT on microstructural evolution

After DCT, the alloy will shrink to produce internal stress. The change of EHEA diffraction peak intensity after different DCT times is observed by XRD patterns, which is caused by the deflection of grain orientation to different crystal planes. The internal stress generated by DCT is also common in other FeCoNi series high-entropy alloys^[10]. At the same time, a rightward shift of the diffraction peaks of the FCC and B2 phases can be observed in the XRD spectrum. The residual stress generated after DCT causes lattice anisotropy contraction, which reduces the lattice constant^[16]. DCT increases the internal strain of EHEAs, which in turn leads to changes in the lattice constant and interplanar spacing of EHEAs. The micro-stress produced after DCT is measured to be compressive stress^[17]. The as-cast $\text{AlCoCrFeNi}_{2.1}$ EHEAs

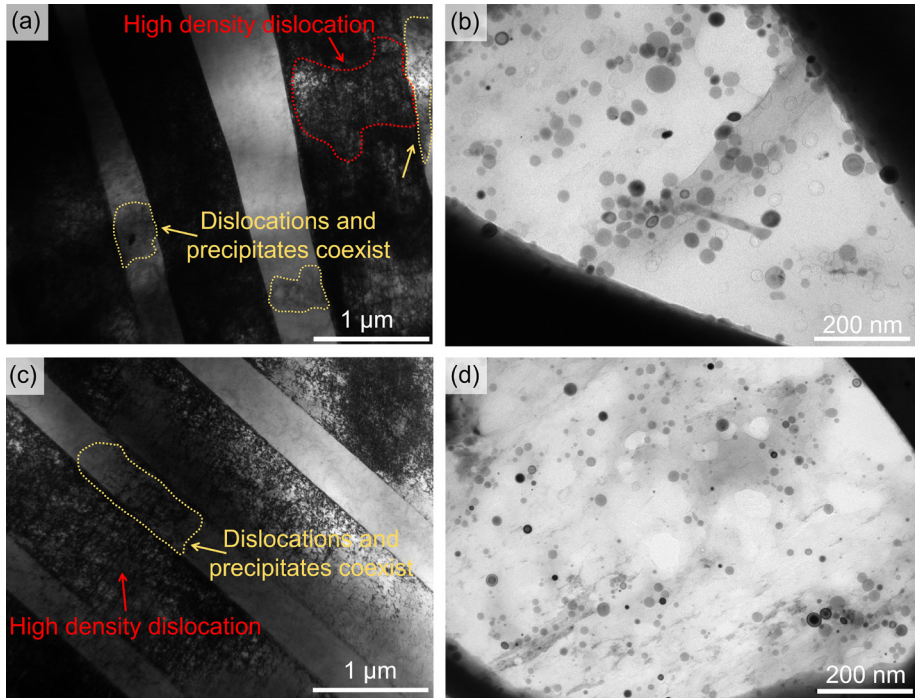


Fig. 7: TEM images of EHEA samples with different DCT times: (a-b) DCT-24; (c-d) DCT-36

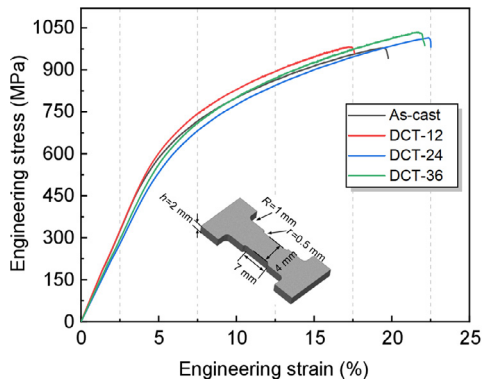


Fig. 8: Room temperature tensile stress-strain curves of AlCoCrFeNi_{2.1} EHEAs

Table 1: Mechanical properties of AlCoCrFeNi_{2.1} under different DCT times

| Alloy | DCT time (h) | Tensile strength (MPa) | Elongation (%) |
|--------|--------------|------------------------|----------------|
| AC | 0 | 978.32 | 19.43 |
| DCT-12 | 12 | 982.38 | 17.23 |
| DCT-24 | 24 | 1,014.73 | 22.35 |
| DCT-36 | 36 | 1,034.51 | 21.72 |

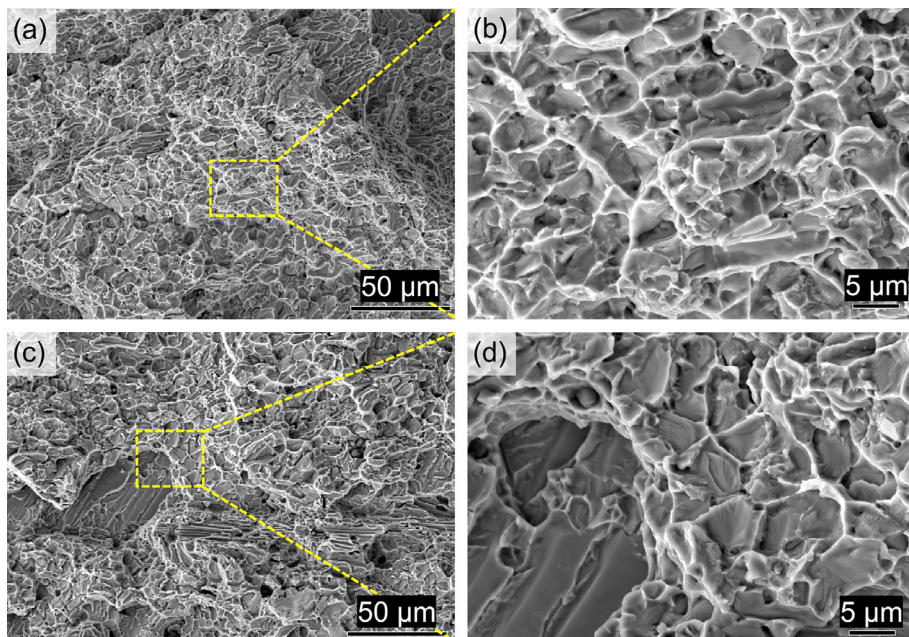


Fig. 9: Fracture morphology of AlCoCrFeNi_{2.1} EHEA stretched at room temperature: (a-b) as-cast; (c-d) DCT-36

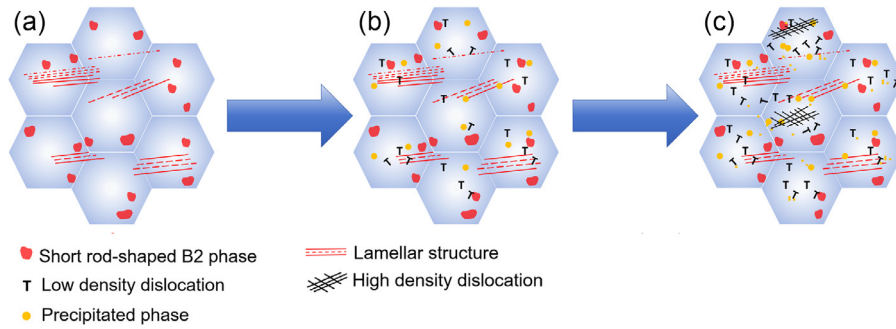


Fig. 10: Schematic diagram of microstructural changes in deformation and the generation mechanism of dislocation precipitation during DCT: (a) as-cast; (b) at the beginning of DCT; (c) after completion of DCT

are composed of lamellar eutectic structure and blocky non-eutectic structure, as shown in Fig. 10(a). Both of them include FCC phase and short rod B2 phase. In Fig. 10(b), the black “T” marks represent dislocations. The DCT process rapidly cools the EHEAs from 298 K to 77 K, resulting in a significant extrusion shrinkage effect between the EHEAs grains. The lattice distortion is serious and the dislocation density increases gradually. DCT induces microplastic deformation in high entropy alloys, causing localized relaxation of the tensile thermal stress. In Fig. 10(c), dislocation networks are formed when the samples undergo a prolonged DCT. During the rapid cooling process in a liquid nitrogen environment, atoms or grains undergo shrinkage without sufficient time for rearrangement and uniform distribution, resulting in dislocations in the lattice structure. Due to crystal defects, plastic deformation and constraints between grains, the dislocation network remains within the grains. It should be added that in this DCT strengthening mechanism, when there is no defect or plastic deformation area during the cooling process, the stress generated during the initial cooling process will be completely restored when it is reheated to room temperature. Therefore, such areas should not contain any new defects or plastic deformation.

The DCT process also promotes the formation of precipitates. According to the XRD results, the lattice parameter of the FCC phase is calculated to be 0.20541 nm, while the lattice parameter of B2 is determined to be 0.20707 nm. The difference in lattice parameters between the two phases is the largest at different DCT times, leading to a non-coherent interface relationship. The atoms are difficult to diffuse at lower temperatures, and the diffusion distance is shortened. The low temperature allows the nanoprecipitate to exist stably [30]. After DCT, the precipitate undergoes a series of changes. In the initial stage, primary large-sized precipitates are generated in the B2 ordered region and exhibit the same composition as the matrix. Considering that the atomic radii of Al and Fe are 0.143 nm and 0.126 nm, respectively, the BCC precipitates are completely coherent with the B2 matrix [33]. The lattice mismatch can be neglected, and the mismatch strain energy and interface energy are extremely low. The yellow marker in Fig. 10(b) represents the precipitate. After DCT-12, the presence of dislocations provides more nucleation sites for the precipitate, resulting in an increase in the number of precipitates. Due to the positive

mixing enthalpy between Fe and Al, the mismatch strain energy is low, but the interface energy is relatively high [34]. Subsequently, in DCT-24 and DCT-36 samples, it is confirmed that the increase in the density of dislocations significantly enhances the number and density of precipitate nucleation. The increase of DCT time tends to produce smaller and more stable BCC precipitates, which can effectively reduce the interface energy. After different DCT times, it is observed that all the precipitates in the sample show BCC structure. This suggests that the transition from B2 to BCC is dynamically delayed [19]. Meanwhile, the mismatch in thermal expansion coefficient and elastic modulus between the precipitate and AlCoCrFeNi_{2.1} EHEA matrix leads to the emergence of many nucleation sites for dislocation in the metal matrix, resulting in a high density of dislocations [28]. In summary, prolonging DCT time leads to an increase in both the density of dislocations and the volume fraction of precipitates within the microstructure.

4.2 Effect of DCT on mechanical properties

The generation of dislocations and precipitates during DCT is crucial for improving the mechanical properties of EHEAs. The evolution of dislocation morphology is attributed to the increase of plastic deformation and the gradual accumulation of internal stress in the alloy with the extension of DCT time. During the DCT, the strain density displayed in the EBSD data was observed, demonstrating the continuous accumulation of strain around the grain boundary. It is worth noting that no deformation twins are observed in all samples after DCT, indicating that AlCoCrFeNi_{2.1} EHEA only experiences microplastic deformation dominated by dislocations during DCT. After substituting the EBSD data obtained from DCT into the calculation equation [36] for microstrain, the results can be obtained:

$$\beta = \frac{k\lambda}{D\cos\theta} + 4\epsilon\tan\theta \quad (1)$$

D is the grain size, and θ is the radian value of the peak. λ is the wavelength. k is a constant, generally 0.89. β is broadening, and ϵ is microscopic stress. With the extension of DCT time, the micro-strain is increased from 0.03% of the as-cast state to 2.84% of DCT-12, 3.27% of DCT-24, and 3.91% of DCT-36.

In order to evaluate the effect of dislocation strengthening on the mechanical properties of alloys, the contribution of

dislocation strengthening (σ_D) is calculated using the Taylor law as follows^[23]:

$$\sigma_D = M\alpha Gb\rho^{0.5} \quad (2)$$

The Taylor factor (M) for FCC alloy and BCC alloy is 3.06 and 2.71, respectively^[26]. The GNDs in a specific region, denoted as ρ . The dimensionless pre-factor (α) is approximately 0.2 for the FCC phase and about 0.24 for the BCC phase^[13,24]. The shear modulus (G) is 81 GPa for the FCC phase and 57 GPa for the BCC phase. The Burgers vector length (b) is measured as 0.254 nm for the FCC phase and 0.248 nm for the BCC phase^[26]. By combining the contributions of FCC and BCC phases, the strengthening effect caused by dislocations is directly proportional to the calculated dislocation density. KAM values can be converted to GNDs by the following equation^[20-21]:

$$\rho_{\text{GND}} = \frac{2\text{KAM}}{u\mathbf{b}} \quad (3)$$

where u equals to the scan step size and \mathbf{b} is the Burgers vector which is consistent with above data^[26]. The GNDs of the FCC and BCC phases can be calculated through Eq. (3). After calculation, the as-cast AlCoCrFeNi_{2.1} EHEA dislocation density is very low and almost does not play a role in strengthening. The GNDs increase to $0.40 \times 10^{14} \text{ m}^{-2}$, $0.69 \times 10^{14} \text{ m}^{-2}$, and $0.71 \times 10^{14} \text{ m}^{-2}$ for DCT-12, DCT-24, and DCT-36. The interaction between these dislocations plays an important role in improving the yield strength of the alloy. By introducing the obtained GNDs into Eq. (1), the strengthening effects of dislocations after DCT-12, DCT-24, and DCT-36 are as follows: 34.07 MPa, 56.81 MPa, and 57.63 MPa.

As the temperature rapidly decreases, the density of dislocations in the EHEA tends to increase, accompanied by the emergence of numerous precipitates. The presence of precipitations also contributes to the increase of tensile strength of alloys after DCT. Due to the uneven distribution of these nanoprecipitate, additional resistance is generated, causing moving dislocations to stagnate or accumulate and further creating higher stress at grain boundaries. Meanwhile, the motion of dislocation is impeded by precipitates, causing them to elongate and accumulate when encountering these phases. The morphology of dislocations changes from short-line shape to dislocation network, which further limits the movement of dislocations and enhances the ability of EHEAs to resist deformation. The distribution of precipitates is relatively uniform, and its volume fraction can be determined by the following equation^[25]:

$$f_v = \frac{1}{2\left[\left(\frac{\lambda}{2r} + 1\right)^3\right]} \quad (4)$$

where f_v represents the volume fraction, λ is the interparticle spacing of precipitates, and r stands for the average radius of particles. Based on the analysis of the images in Figs. 6(f), 7(b), and 7(d), the average radii of the precipitated phases of DCT-12, DCT-24, and DCT-36 are 71.42 nm, 57.52 nm, and 31.25 nm. The corresponding precipitation phase spacings are 425.36 nm, 220.51 nm, and 156.13 nm. Using these

information and equations, the volume fraction of precipitates can be calculated to increase from 0.79% for DCT-24 to 1.11% for DCT-36. The contribution of precipitation strengthening (ρ_p) is calculated by the following equation^[32]:

$$\rho_p = M \frac{\eta G b}{\pi \sqrt{1-\nu}} \frac{\ln(2r/b)}{\lambda} \quad (5)$$

When the precipitated phase is not arrayed, $\eta=0.8$. ν is the Poisson ratio of AlCoCrFeNi series high entropy alloys, close to 0.3. Incorporating above parameters into Eq. (5), the precipitate phase enhancement capacity of DCT at different times can be obtained, which is 2.09 MPa for DCT-12, 3.87 MPa for DCT-24, and 4.86 MPa for DCT-36. The calculated results of dislocation and precipitation strengthening are close to the actual tensile test results.

In addition, the plasticity of AlCoCrFeNi_{2.1} EHEAs is significantly improved after DCT. The fracture of the as-cast AlCoCrFeNi_{2.1} EHEA in the tensile test is mainly due to the large hardness difference between the FCC phase and the B2 phase, resulting in stress concentration at the interface. The higher plasticity after DCT can be attributed to the following factors: the low stacking fault energy of the FCC phase, combined with the BCC/B2 coherent interface, promotes the uniform distribution of stacking fault energy in the entire eutectic lamellar without causing stress concentration at the interface. Dislocations also play a role in improving plasticity. When the dislocation network is subjected to tensile stress, deformation can occur without breaking^[27]. This allows for unimpeded movement of dislocations in the FCC phase, resulting in its hardening and improved resistance to deformation. DCT narrows the gap between the FCC and B2 phases, allowing both phases to resist deformation synergistically. Coherent precipitation strengthening also plays a crucial role in conferring unique mechanical properties to EHEAs, including exceptional plasticity at low and room temperature^[23]. The combined effect of dislocations and precipitates significantly enhances the ductility of EHEAs. Therefore, the synergistic effect of dislocations and precipitates after DCT improves the tensile strength and ductility of AlCoCrFeNi_{2.1} EHEAs.

The morphology of the tensile fracture was observed by SEM, and it is found that the fracture mode of the eutectic high-entropy alloy after DCT-36 is ductile and brittle composite fracture. The formation mechanism of these grooved, flat, layered or skeleton-like microstructures can be reasonably inferred from the FCC/B2 (BCC) composite structures present in the as-cast and DCT AlCoCrFeNi_{2.1} EHEAs. During the deformation process at room temperature, the hard B2 phase undergoes minimal deformation or slight deformation, while the soft FCC phase undergoes significant changes upon stretching. Consequently, the FCC phase gradually becomes thinner and moves in the direction of the tensile stress, with the B2 phase remaining almost undeformed at the bottom of the trench^[35]. After DCT-36, the internal stress increases, resulting in a change in the crystal lattice. There are obvious differences in the distribution of grooved, flat, and layered

microstructures. According to the second phase strengthening mechanism, the formation of high-density BCC precipitates enhances the tensile strength of EHEAs. The BCC precipitate phase is uniformly distributed and does not accumulate at the grain boundaries. Therefore, it does not reduce the plasticity of EHEAs. The change of fracture morphology in both the FCC phase and B2 phase provides support for the principle that DCT that can improve the mechanical properties of AlCoCrFeNi_{2.1} EHEAs.

5 Conclusions

In this study, the microstructure and mechanical properties of AlCoCrFeNi_{2.1} EHEA with varying duration of deep cryogenic treatment (DCT) were extensively investigated. The DCT process produces high-density dislocations and uniformly distributed precipitates in EHEAs. This method provides a promising design strategy for optimizing the comprehensive mechanical properties of EHEAs. The conclusions are summarized as follows:

(1) DCT causes dislocations in AlCoCrFeNi_{2.1} EHEAs, and the dislocation density increases with the extension of DCT time. The dislocation density of the alloy after DCT for 36 h increases to a maximum of $0.71 \times 10^{14} \text{ m}^{-2}$. After DCT for 24 h, the dislocation morphology also changes significantly, and the low-density dislocation lines are entangled together to become dislocation networks or dislocation walls.

(2) DCT produces precipitates in AlCoCrFeNi_{2.1} EHEAs. The BCC coherent precipitates are formed in the B2 matrix. With the extension of DCT time, the volume fraction of precipitates increases, and the size of newly formed precipitates significantly decreases. The average radii of the precipitated phases after DCT for 12 h, 24 h, and 36 h are 71.42 nm, 57.52 nm, and 31.25 nm, respectively.

(3) AlCoCrFeNi_{2.1} EHEAs achieve the best comprehensive mechanical properties after DCT for 36 h. Its tensile strength is 1,034.51 MPa. The plasticity reaches 21.72%, which is 11.79% higher than that of the as-cast state. AlCoCrFeNi_{2.1} EHEAs are more suitable for engineering applications after being strengthened by DCT process.

Acknowledgments

This study was financially supported by the National Natural Science Foundation of China (Nos. 52301061, 52204394), the Joint Fund Project of Science and Technology Plan of Liaoning Province (No. 2023-MSLH-250), and the Science and the Technology Program of Liaoning Provincial Department of Education (No. JYTQN2023286).

Conflict of interest

The authors declare that they have no known competing financial interests or personal relationships that could have appeared to influence the work reported in this paper.

References

- [1] Wei S, Wang C, Peng W, et al. Effects of process parameters and annealing on microstructure and properties of CoCrFeMnNi high entropy alloy coating prepared by plasma cladding. *China Foundry*, 2023, 20(6): 491–502.
- [2] Shi P, Ren W, Zheng T, et al. Enhanced strength-ductility synergy in ultrafine-grained eutectic high-entropy alloys by inheriting microstructural lamellae. *Nature Communications*, 2019, 10(1): 489.
- [3] Miracle D B, Senkov O N. A critical review of high entropy alloys and related concepts. *Acta Materialia*, 2017, 122: 448–511.
- [4] Lu Y P, Dong Y, Jiang H, et al. Promising properties and future trend of eutectic high entropy alloys. *Scripta Materialia*, 2020, 187: 202–209.
- [5] Qi H, Li G L, Zhang W, et al. Effect of TiO₂ nano-ceramic particles on microstructure and mechanical properties of Al_{0.4}CoCrFe₂Ni₂ high entropy alloy. *China Foundry*, 2022, 19(6): 528–534.
- [6] Huo W, Zhou H, Fang F, et al. Microstructure and mechanical properties of CoCrFeNiZr_x eutectic high entropy alloys. *Materials & Design*, 2017, 134: 226–233.
- [7] Tan Y, Li J, Wang J, et al. Seaweed eutectic-dendritic solidification pattern in a CoCrFeNiMnPd eutectic high entropy alloy. *Intermetallics*, 2017, 85: 74–79.
- [8] He F, Wang Z, Cheng P, et al. Designing eutectic high entropy alloys of CoCrFeNiNb_x. *Journal of Alloys and Compounds*, 2016, 656: 284–289.
- [9] Nassar A, Mullis A, Cochrane R, et al. Rapid solidification of AlCoCrFeNi_{2.1} high-entropy alloy. *Journal of Alloys and Compounds*, 2022, 900: 163350.
- [10] Liu J Q, Wang H M, Li G R, et al. Microstructure and improved plasticity of (FeCoNi_{1.5}CrCu)_p/Al composites subject to adjusted deep cryogenic treatment (DCT). *Journal of Alloys and Compounds*, 2022, 895: 162690.
- [11] Li J, Zhou J, Sun Y, et al. Study on mechanical properties and microstructure of 2024-T351 aluminum alloy treated by cryogenic laser peening. *Optics & Laser Technology*, 2019, 120: 105670.
- [12] Xie S C, Lv Q Y, Zhang W, et al. Effect of cryogenic treatment on microstructure and mechanical properties of Al_{0.6}CrFe₂Ni₂ dual-phase high-entropy alloy. *Metals*, 2023, 13(2): 195.
- [13] He J Y, Wang H, Huang H L, et al. A precipitation-hardened high entropy alloy with outstanding tensile properties. *Acta Materialia*, 2016, 102: 187–196.
- [14] Peng P, Feng X, Li S, et al. Effect of heat treatment on microstructure and mechanical properties of as-cast AlCoCrFeNi_{2.1} eutectic high entropy alloy. *Journal of Alloys and Compounds*, 2023, 939: 168843.
- [15] Sheng H F, Gong M, Peng L M. Microstructural characterization and mechanical properties of an Al_{0.5}CoCrFeCuNi high-entropy alloy in as-cast and heat-treated/quenched conditions. *Materials Science and Engineering: A*, 2013, 567: 14–20.
- [16] Wang Y, Liu B, Yan K, et al. Probing deformation mechanisms of a FeCoCrNi high entropy alloy at 293 and 77 K using in situ neutron diffraction. *Acta Materialia*, 2018, 154: 79–89.
- [17] Sri Siva R, Shunmuga Priyan M. Residual stress and wear studies of deep cryogenically treated SAE 52100 bearing steel. *Advanced Materials Proceedings*, 2019, 4(1): 48–54.
- [18] Tao X, Zhang Z, Zhang B, et al. Plasma sprayed CoNiCrMoNb(BSi) high-entropy amorphous alloy coating: The effect of spraying power on microstructure, mechanical and tribological properties. *Materials Chemistry and Physics*, 2024, 314: 128887.

- [19] Jung J G, Jung M, Lee S M, et al. Cu precipitation kinetics during martensite tempering in a medium C steel. *Journal of Alloys and Compounds*, 2013, 553: 299–307.
- [20] Kubin L P, Mortensen A. Geometrically necessary dislocations and strain-gradient plasticity: A few critical issues. *Scripta Materialia*, 2003, 48(2): 119–125.
- [21] Xie J, Zhang Z, Liu S, et al. Designing new low alloyed Mg-RE alloys with high strength and ductility via high-speed extrusion. *International Journal of Minerals, Metallurgy and Materials*, 2023, 30(1): 82–91.
- [22] Konijnenberg P J, Zaefferer S, Raabe D. Assessment of geometrically necessary dislocation levels derived by 3D EBSD. *Acta Materialia*, 2015, 99: 402–414.
- [23] Taylor G I. Plastic strain in metals. *Journal of the Institute of Metals*, 1938, 62: 307–324.
- [24] Otto F, Dlouhý A, Somsen C, et al. The influences of temperature and microstructure on the tensile properties of a CoCrFeMnNi high entropy alloy. *Acta Materialia*, 2013, 61(15): 5743–5755.
- [25] Zou C, Chen Z, Guo E, et al. A nano-micro dual-scale particulate-reinforced copper matrix composite with high strength, high electrical conductivity and superior wear resistance. *RSC Advances*, 2018, 8(54): 30777–30782.
- [26] Ren J, Zhang Y, Zhao D, et al. Strong yet ductile nano lamellar high entropy alloys by additive manufacturing. *Nature*, 2022, 608(7921): 62–68.
- [27] Fan L, Yang T, Zhao Y, et al. Ultrahigh strength and ductility in newly developed materials with coherent nano lamellar architectures. *Nature Communications*, 2020, 11(1): 6240.
- [28] Sanaty-Zadeh A. Comparison between current models for the strength of particulate-reinforced metal matrix nanocomposites with emphasis on consideration of Hall-Petch effect. *Materials Science and Engineering: A*, 2012, 531: 112–118.
- [29] Qi H, Lv Q Y, Li G L, et al. Effect of cryogenic treatment on B2 nanophase, dislocation and mechanical properties of $Al_{1.4}CrFe_2Ni_2$ (BCC) high entropy alloy. *Materials Science and Engineering: A*, 2023, 878: 145183.
- [30] Jiang L, Cao Z Q, Jie J C, et al. Effect of Mo and Ni elements on microstructure evolution and mechanical properties of the $CoFeNi_xVMo_y$ high entropy alloys. *Journal of Alloys and Compounds*, 2015, 649: 585–590.
- [31] Buzolin R H, Masswohl M, Ferraz F M B, et al. Microstructure refinement of a cast high entropy alloy by thermomechanical treatments. *Materials Science and Engineering: A*, 2023, 872: 144931.
- [32] He J Y, Wang H, Wu Y, et al. Precipitation behavior and its effects on tensile properties of FeCoNiCr high-entropy alloy. *Intermetallics*, 2016, 79: 41–52.
- [33] Smith D W. *Inorganic substances: A prelude to the study of descriptive inorganic chemistry*. Cambridge University Press, 1990.
- [34] Takeuchi A, Inoue A. Classification of bulk metallic glasses by atomic size difference, heat of mixing and period of constituent elements and its application to characterization of the main alloying element. *Materials Transactions*, 2005, 46(12): 2817–2829.
- [35] Shu T, Hu N, Liu F, et al. Nanoparticles induced intragranular and dislocation substructures in powder bed fusion for strengthening of high entropy-alloy. *Materials Science and Engineering: A*, 2023, 878: 145110.
- [36] Li D F, Davies C M, Zhang S Y, et al. The effect of prior deformation on subsequent microplasticity and damage evolution in an austenitic stainless steel at elevated temperature. *Acta Materialia*, 2013, 61(10): 3575–3584.